



Low-metallicity Nova Explosions: A Site for Weak *rp*-process Nucleosynthesis

Athanasios Psaltis^{1,2} , Jordi José^{3,4} , Richard Longland^{2,5} , and Christian Iliadis^{2,6} ¹ Department of Physics, Duke University, Durham, NC 27710, USA; psaltis.tha@duke.edu² Triangle Universities Nuclear Laboratory, Duke University, Durham, NC 27710, USA³ Departament de Física, EEBE, Universitat Politècnica de Catalunya, c/Eduard Maristany 10, E-08930 Barcelona, Spain⁴ Institut d'Estudis Espacials de Catalunya, c/Estev Terradas 1, E-08860 Castelldefels, Spain⁵ Department of Physics, North Carolina State University, Raleigh, NC 27695, USA⁶ Department of Physics & Astronomy, University of North Carolina at Chapel Hill, NC 27599-3255, USA

Received 2025 April 17; revised 2025 May 13; accepted 2025 June 1; published 2025 July 1

Abstract

Classical novae are common cataclysmic events involving a binary system of a white dwarf and a main-sequence or red giant companion star. In metal-poor environments, these explosions produce ejecta differently from their solar counterparts due to the accretion of subsolar-metallicity material onto the white dwarf. In particular, it has been suggested that the nucleosynthesis flow in such low-metallicity nova explosions extends up to the Cu–Zn region, much beyond the expected endpoint, around Ca, predicted for solar-metallicity classical novae. This behavior resembles a weak *rp*-process, and such nuclear activity has never been observed in accreting white dwarf binaries with typical accretion flows. In this work, we study the characteristics of the weak *rp*-process for four nova models with metallicities $Z = 2 \times 10^{-9}$, 10^{-7} , 2×10^{-6} , and 2×10^{-5} , and explore the impact of the nuclear physics uncertainties via a Monte Carlo sensitivity study. We identify nuclear reactions whose uncertainties affect the production of intermediate-mass nuclei under these conditions. These reactions and relevant nuclear quantities are targets for measurements at stable or radioactive beam facilities to reduce their rate uncertainties.

Unified Astronomy Thesaurus concepts: Classical novae (251); Explosive nucleosynthesis (503); Nuclear astrophysics (1129); Nuclear reaction cross sections (2087)

1. Introduction

Classical novae (see J. José & S. N. Shore 2008; S. Starrfield et al. 2008, 2012, 2016; J. José 2016; L. Chomiuk et al. 2021 for some reviews) are stellar thermonuclear explosions, occurring at a rate of $\approx 30\text{--}80 \text{ yr}^{-1}$ in our Galaxy (A. W. Shafter 2017). Only $\approx 5\text{--}10$ are detected annually,⁷ as many are obscured by interstellar dust. These events occur in binary systems, where a white dwarf accretes material from a main-sequence or a red giant companion. The material from the companion star accumulates onto the CO or ONe white dwarf and triggers a thermonuclear explosion on its surface. The nucleosynthesis endpoint in classical novae is predicted by models and confirmed by observations to be around $A \sim 40$ (calcium). Each nova outburst ejects only $\sim 10^{-7}\text{--}10^{-4} M_{\odot}$ of material into the interstellar medium, which is why they are not considered major contributors to Galactic chemical evolution. However, they can be significant Galactic contributors of ^{13}C , ^{15}N , and ^{17}O (J. José 2016). In addition, ^7Li , which originates from the decay of ^7Be , has been suggested to be mainly produced in nova explosions (S. Starrfield et al. 2020), but this remains a subject of ongoing debate (J. José et al. 2020).

Early in Galactic history, low- and even zero-metallicity (Population III) stars (A. Stacy & V. Bromm 2013; A. Stacy et al. 2016; R. S. Klessen & S. C. O. Glover 2023) likely formed binary systems that could have produced a unique type

of stellar explosion, with an energy output between a classical nova⁸ and a supernova. This low-metallicity binary system is expected to behave differently from a classical nova with solar metallicities. J. José et al. (2007) proposed that, unlike classical novae that produce elements only up to Ca, low-metallicity novae could synthesize heavier elements, reaching the Cu–Zn region through a sequence of (*p*, γ) radiative captures and β^+ decays. The distinguishing features between the two environments are the higher peak temperature reached in the latter, along with the dredging up of freshly synthesized material from the interior of the red giant, which is transferred in the white dwarf envelope, triggering a breakout from the hot CNO cycles (M. Wiescher et al. 2010; C. Iliadis 2015).

Beyond the work of J. José et al. (2007), the impact of metallicity on nova explosions has been explored in several studies (L. Piersanti et al. 2000; S. Starrfield et al. 2000; K. J. Shen & L. Bildsten 2007, 2009; H.-L. Chen et al. 2019), though typically not for values below $Z = 10^{-6}$. Most recently, A. J. Kemp et al. (2024) investigated the role of novae in Galactic chemical evolution using binary population synthesis models across a range of metallicities from $Z = 10^{-4}$ to 3×10^{-2} . Their results suggest that both the nova rate and the amount of material ejected into the interstellar medium are inversely proportional to the metallicity of the system.

Low-metallicity environments—such as the Milky Way halo, the Magellanic Clouds, globular clusters (GCs), and dwarf galaxies—are expected to host a larger fraction of binary systems capable of producing nova explosions. For

⁷ Public database of Galactic novae “galnovae” available at <https://github.com/Bill-Gray/galnovae/>.



Original content from this work may be used under the terms of the [Creative Commons Attribution 4.0 licence](https://creativecommons.org/licenses/by/4.0/). Any further distribution of this work must maintain attribution to the author(s) and the title of the work, journal citation and DOI.

⁸ In this paper, we use the following nomenclature for classical nova explosions with different metallicities: solar-metallicity nova refers to a white dwarf accreting solar-composition material. Primordial nova describes a system where a Population III star transfers material to a white dwarf. Low-metallicity nova encompasses all the other cases where the companion star has a subsolar metallicity.

Table 1
Model Parameters for the Nova Simulations in This Study

Property	Model Z2e-9	Model Z1e-7	Model Z2e-6	Model Z2e-5
Composition of accreted material	solar/ 10^7	solar/ 2×10^5	solar/ 10^4	solar/ 10^3
Metallicity of accreted material	$Z = 2 \times 10^{-9}$	$Z = 10^{-7}$	$Z = 2 \times 10^{-6}$	$Z = 2 \times 10^{-5}$
$M_{\text{env}} (10^{-5} M_{\odot})$	3.36	1.78	1.38	1.28
$P_{\text{max}} (10^{19} \text{ dyn cm}^{-2})$	33.9	18.1	14.1	13.2
$T_{\text{max}} (\text{MK})$	466	385	364	359
$M_{\text{ejec}} (10^{-5} M_{\odot})$	2.71	1.43	1.11	1.03
$v_{\text{ejec}} (\text{km s}^{-1})$	4239	3950	4068	4140

Note. All nova models involve an ONe white dwarf of $M_{\text{WD}}^{\text{ini}} = 1.35 M_{\odot}$, $R_{\text{WD}} = 2260 \text{ km}$, $L_{\text{ini}} = 10^{-2} L_{\odot}$, and $M_{\text{acc}} = 2 \times 10^{-10} M_{\odot} \text{ yr}^{-1}$.

example, the Large and Small Magellanic Clouds have mean metallicities of $[\text{Fe}/\text{H}] \approx -0.33(30)$ and $[\text{Fe}/\text{H}] \approx -0.83(30)$, respectively (V. Hócdé et al. 2023). In such environments, novae are predicted to eject more massive shells, potentially enhancing their contribution to Galactic chemical evolution. These low-metallicity novae may have also left an imprint in the inventory of presolar stardust grains (S. Amari et al. 2001).

Extending the analysis of J. José et al. (2007), who modeled novae with accreted material matching the lowest stellar metallicities observed, we find that a more detailed study is necessary. Their reaction network, coupled to their hydrodynamic code, was limited to 270 nuclei and 1400 reactions (see Section 3 for details). Many thermonuclear reaction rates in the mass range $A = 30\text{--}50$ have large uncertainties that eventually affect the final abundance pattern. Investigating these nuclear uncertainties in a hydrodynamical model is prohibitive due to the computational expense of the calculations. Instead, it is preferred to perform postprocessing calculations using an extended nuclear reaction network and a temperature and density profile extracted from a hydrodynamical simulation (see the work by C. Iliadis et al. 2002).

Although classical novae have been observed from γ rays to radio waves (L. Chomiuk et al. 2021), there is no direct detection of a Population III star ($Z = 0$),⁹ or a Population III binary system. T. Hartwig et al. (2015) have provided an estimate of $\sim 10^6$ Population III survivors in the halo of the Milky Way, which have not yet been observed but would likely be the target of the next generation of space telescopes at high z (K. Nakajima & R. Maiolino 2022). To strengthen our theoretical framework, it is crucial to improve our understanding of the nucleosynthesis processes and observational signatures involving low-metallicity nova explosions. By refining our theoretical predictions, we aim to establish a solid foundation for interpreting the observed abundances in these systems, ensuring that we are prepared to draw meaningful conclusions from future detections with next-generation space telescopes.

In the present work, we aim to answer the following two questions: (1) what does the nucleosynthesis in low-metallicity novae look like, and (2) how do the nuclear physics uncertainties affect it? To achieve this, we have calculated the nucleosynthesis of four 1D low-metallicity nova models, with $Z = 2 \times 10^{-9}$, 10^{-7} , 2×10^{-6} , and 2×10^{-5} , building on

the work of J. José et al. (2007). These calculations use an extended nuclear network coupled to a state-of-the-art reaction rate library. We have also performed Monte Carlo reaction network studies to explore the impact of thermonuclear reaction rate uncertainties on the resulting nucleosynthesis. Answering these questions will help us better understand nucleosynthesis early in Galactic history and offer a guide for the experimental nuclear physics community to pursue measurements of key reactions of astrophysical interest at stable and radioactive ion beam facilities.

This paper is structured as follows: In Section 2, we discuss the specifics of low-metallicity nova explosions and present the different hydrodynamical profiles that we selected for our study. Section 3 will provide a detailed description of the nucleosynthesis processes that occur in these nova explosions, and in Section 4, we present our reaction network setup for the Monte Carlo sensitivity study. In Sections 5 and 6, we present our results, and finally, conclude and discuss our results.

2. Hydrodynamical Simulations of Low-metallicity Nova Explosions

In the present work, we revisit the two low-metallicity nova models presented in J. José et al. (2007), and we expand our reach in the metallicity phase space by including two more models. Their metallicity values Z are 2×10^{-9} , 10^{-7} , 2×10^{-6} , and 2×10^{-5} . For more details, see Table 1. These correspond to spectroscopic values $[\text{Fe}/\text{H}] = -7$, -5.4 , -4 , and -3 , respectively. The lowest-metallicity nova model was selected to match one of the most metal-deficient stars observed, SMSS J031300.36–67083 (S. C. Keller et al. 2014). Models Z1e-7 and Z2e-6 correspond to Models A and B of J. José et al. (2007). All models were computed using the 1D implicit Lagrangian hydrodynamic code SHIVA (see J. José & M. Hernanz 1998; J. José 2016 for details), which has been widely used to model classical nova explosions and type I X-ray bursts. The code self-consistently couples hydrodynamics with an extensive nuclear reaction network to simulate thermonuclear runaways and the resulting nucleosynthesis. SHIVA incorporates energy generation from nuclear reactions, convective transport, and the effects of a degenerate equation of state, making it a robust tool for studying nova outbursts across different metallicities.

As discussed in J. José et al. (2007), the choice of a rather massive white dwarf ($M_{\text{WD}} = 1.35 M_{\odot}$) stems from the need to explore the nucleosynthetic endpoint of these explosions, since more massive white dwarfs lead to higher peak temperatures during the explosion phase, due to the higher pressure at the base of the envelope, and eventually a more violent outburst. For the present work, we did not compute models for a variety

⁹ Recent observations using JWST have pointed to possible signatures of Population III stars at redshift $z = 10.6$ (R. Maiolino et al. 2024). One of the most metal-deficient stars observed, SMSS J031300.36–670839.3 has an $[\text{Fe}/\text{H}] = -7.1$ (S. C. Keller et al. 2014), where $[\text{Fe}/\text{H}] = \log_{10} \left(\frac{N_{\text{Fe}}}{N_{\text{H}}} \right)_{\star} - \log_{10} \left(\frac{N_{\text{Fe}}}{N_{\text{H}}} \right)_{\odot}$.

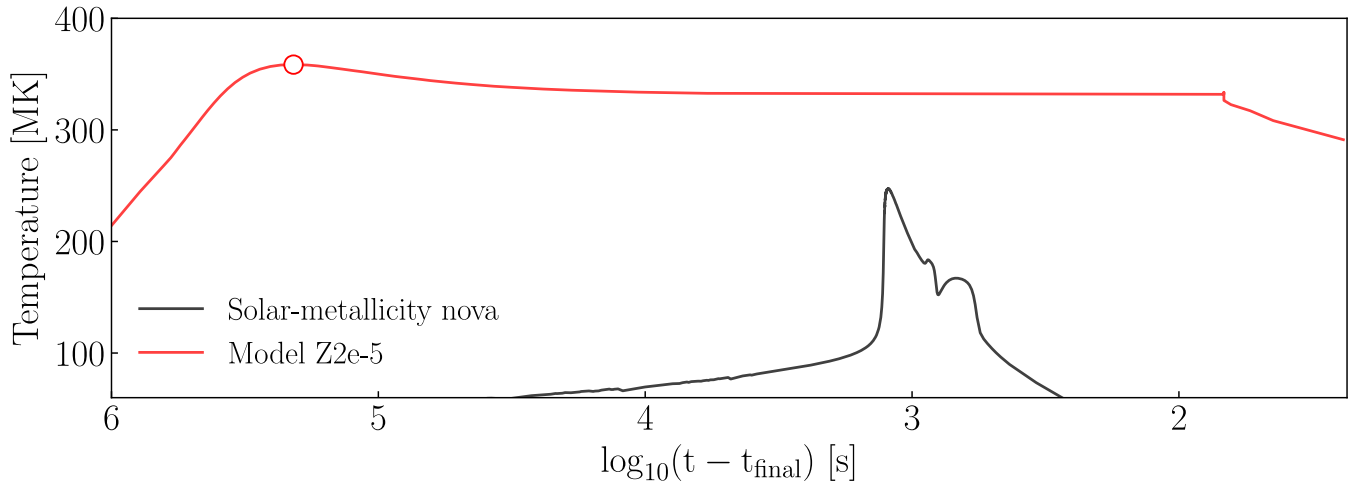


Figure 1. Temperature evolution of the innermost shell for a low-metallicity nova (model Z2e-5, red) and a solar-metallicity ONe nova (black). Note the significantly higher peak and longer duration of the temperatures in the low-metallicity model. The white circle indicates the beginning of the postprocessing calculation at $T = T_{\max}$.

of white dwarf masses since our main goal was to study the extent of nuclear activity in low-metallicity novae. A comprehensive characterization of the outcomes of novae as a function of white dwarf mass, initial luminosity, and mass-accretion rate is beyond the scope of this paper and will be addressed in future work.

Table 1 shows the parameters of the low-metallicity nova models computed in this work. The quantities M_{wd} and R_{wd} are, respectively, the initial values of the white dwarf mass and radius, after relaxation of the initial model, just when accretion sets in, L_{ini} is the initial white dwarf luminosity, M_{acc} is the mass-accretion rate, and M_{env} is the final mass of the accreted envelope when the thermonuclear runaway begins. The quantities P_{max} and T_{max} are, respectively, the maximum pressure and temperature achieved at the ignition shell, and M_{ejec} and v_{ejec} are the mass and mean velocity of the ejecta, respectively. The models reach a peak temperature T_{max} , between 359 and 466 MK, which is significantly higher than the typical range of 100–300 MK observed in solar-metallicity novae (J. José 2016).

From the nuclear physics point of view, the key difference in the models considered here to the usually published solar-metallicity models is not only that the former achieve higher peak temperatures, but the high temperatures are also maintained for a much longer time. We illustrate that feature in Figure 1, where the time evolution of model Z2e-5 is compared with a typical solar-metallicity ONe nova also computed using the SHIVA code (J. José & M. Hernanz 1998; J. José 2016).

Although we assume that the donor star is unevolved in all models, such that the accreted material reflects the original low-metallicity composition, we note that if the donor were evolved, the composition of the transferred material could be enriched. The hydrodynamic models computed assume that the stream of material accreted by the white dwarf has the same metallicity as the secondary star (see Table 1 for the specific values adopted in each model). However, inspired by multidimensional models of mixing at the core–envelope interface through Kelvin–Helmholtz hydrodynamic instabilities, some material is assumed to be dredged up into the innermost layer of the envelope with a characteristic timescale given by the convective turnover time, $\tau_{\text{conv}} \sim 10$ s, as soon as the envelope becomes fully convective (S. A. Glasner et al. 2012, 2007, 1997; J. Casanova et al. 2018,

Table 2
Chemical Composition in the Outermost Layers of an ONe White Dwarf
Based on C. Ritossa et al. (1996)

Isotope	Mass Fraction, X_i
^{12}C	9.16×10^{-3}
^{16}O	5.11×10^{-1}
^{20}Ne	3.13×10^{-1}
^{21}Ne	5.98×10^{-3}
^{22}Ne	4.31×10^{-3}
^{23}Na	6.44×10^{-2}
^{24}Mg	5.48×10^{-2}
^{25}Mg	1.58×10^{-2}
^{26}Mg	9.89×10^{-3}
^{27}Al	1.08×10^{-2}

Note. The composition is taken at mass $M = 1.17 M_{\odot}$.

2016, 2011a, 2011b, 2010). Tests performed with different choices of convective turnover time, from 10 s—very similar to the values reported in the multidimensional calculations of S. A. Glasner et al. and J. Casanova et al.—to 100 s, have shown little impact on the results.

Injecting ^{12}C into the burning region triggers the thermonuclear runaway via the $^{12}\text{C}(p, \gamma)^{13}\text{N}$ reaction, making dredge up of white dwarf and accreted material a crucial component to achieve high nuclear reaction activity. Without the injection of ^{12}C into the burning region, even a hot explosion would not lead to a CNO breakout if the initial composition had very low metallicity. In Table 2, we present the white dwarf core composition, which is based on C. Ritossa et al. (1996). During this dredge-up phase, the mass fraction X_i of each isotope is approximated using the following:

$$X_i = \frac{M_1 X_{\text{old}} + M_2 X_{\text{dredge}}}{M_1 + M_2}, \quad (1)$$

where X_{old} is the mass fraction at the previous time step, X_{dredge} is the composition of the outermost white dwarf layers, as listed in Table 2, $M_2 = M_1 \frac{\Delta t}{\tau}$, where M_1 is the mass of the innermost envelope shell, $\tau = \tau_{\text{conv}} = 10$ s, and Δt is the integration time step. This mixing prescription is assumed both in the hydrodynamical models (J. José et al. 2007) and during

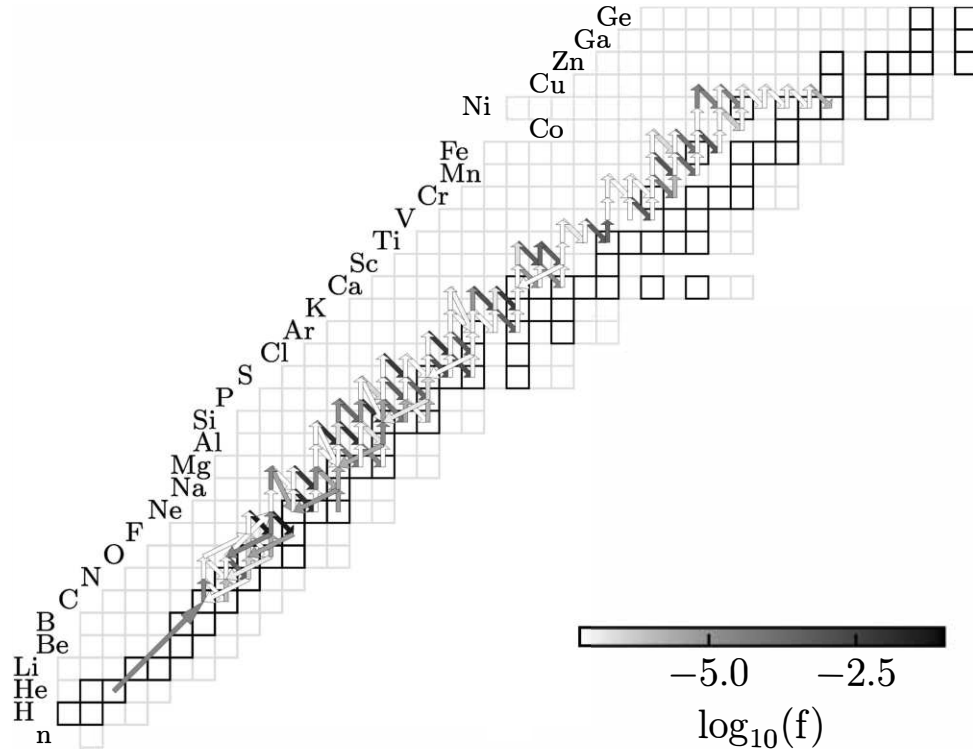


Figure 2. Time-integrated reaction flux for model Z1e-7. The black and gray boxes correspond to the stable and radioactive isotopes of the network, respectively. The color of each flux arrow indicates its magnitude, with darker arrows showing stronger fluxes. See the main text for details.

the nucleosynthesis postprocessing, with modifications that account for the difference between integrating a single-zone thermodynamic profile and a full 1D model, which we discuss in the next section.

3. Nucleosynthesis

The nucleosynthesis in low-metallicity nova explosions was first discussed in J. José et al. (2007). In that work, a network of 270 nuclei (^1H to ^{75}As) was followed through a network of 1400 nuclear reactions, using reaction rates based on experimental information for many stable, and a few radioactive, target reactions, such as for $^{21}\text{Na}(p, \gamma)^{22}\text{Mg}$ (S. Bishop et al. 2003). In this work, we extend the reaction network to 457 nuclei (n to ^{88}Kr) and 4969 nuclear processes. All thermonuclear reaction rates were taken from the STARLIB reaction rate library (A. L. Sallaska et al. 2013; version 6.10).¹⁰ For the reactions that do not have any experimental information, a theoretical rate is used, based on the statistical model calculations of the TALYS code (S. Goriely et al. 2008).

Each network calculation was computed for the duration of the time evolution of the T – ρ profile extracted from the hydrodynamic simulation, between roughly 26 minutes for model Z2e-9 to 58 hr for model Z2e-5. Note that the starting point $t = 0$ of each calculation is when the model reaches T_{max} . At the end of each calculation, we decay all species with $t_{1/2} < 1$ hr to their stable counterparts. The network was integrated using a semi-implicit, second-order Runge–Kutta method (often referred to as “Wagoner’s method,” R. V. Wagoner 1969; R. Longland et al. 2014), ensuring consistency with the hydrodynamical models. However, we

took a slightly different approach with the dredge-up scheme. In the hydrodynamical models, mixing begins when the envelope becomes fully convective and continues until the end of the simulation. However, in our postprocessing approach, we terminated the mixing process much earlier. Specifically, we applied dredging for the following durations: Z2e-9: 7.5 s (1574 s), Z1e-7: 40 s (1476 s), Z2e-6: 75 s (1656 s), and Z2e-5: 75 s (556 s). The numbers in parentheses represent the total duration of dredging in the hydrodynamical simulation. Prolonging the injection of white dwarf core material for the same duration as in the hydrodynamical models—ranging from thousands of seconds to a few days—would have caused the final abundances to be dominated by that material since there is no intrashell mixing in our postprocessing framework. To address this, we tuned the dredge-up time so that the final mass fraction pattern closely matches the mean composition of the ejecta in the hydrodynamical simulation. We emphasize that this tuning is only used to reproduce the overall bulk enrichment, as our one-zone postprocessing framework uses the temperature and density evolution from the SHIVA code for only the innermost shell. The primary goal of our study is to quantify the impact of nuclear reaction rate uncertainties on the production of intermediate-mass nuclei, rather than to make direct comparisons with observed values. In this context, we are confident that this adjustment does not affect the overall conclusions of our study.

Figure 2 presents the total time-integrated reaction flux for model Z1e-7. The net flux from isotope i to isotope j is defined as $f_{ij} = \int \dot{X}_{i \rightarrow j} - \dot{X}_{j \rightarrow i} dt$, where $\dot{X}_{i \rightarrow j}$ is the rate of change of the mass fraction of isotope i by all the reactions that convert it into isotope j . The strongest flux include the (p, γ) reactions followed by β^+ decays.

¹⁰ The STARLIB thermonuclear reaction rate library can be found at <https://starlib.github.io/Rate-Library/>.

In contrast to the rp -process in type I X-ray bursts (H. Schatz et al. 1998), after the breakout of the hot CNO cycle, in the low-metallicity nova scenario, we do not see a sequence of (α, p) and (p, γ) reactions, known as the αp -process (R. K. Wallace & S. E. Woosley 1981). According to Table 1, at the peak temperatures achieved in the models, 359–466 MK, the Coulomb barrier penetrability for α particles remains very low, preventing α captures from becoming dominant. Instead, we get a $(p, \gamma) - \beta^+$ pattern, close to the valley of stability. This also indicates that the critical reactions identified in this study can be accessible by experimental studies.

Nucleosynthesis in a low-metallicity nova setting resembles a weak rp -process, whose extent is between a classical nova and a full rp -process, which has a nucleosynthesis endpoint at the SnSbTe mass region (H. Schatz et al. 1998). Similar nuclear activities have been reported in other studies, such as in L. van Wormer et al. (1994) and J. L. Fisker et al. (2008), but in the context of accreting neutron stars. Such nuclear activity has not been reported for accreting white dwarfs with typical accretion rates of $M_{\text{acc}} = 2 \times 10^{-10} M_{\odot} \text{ yr}^{-1}$. S. A. Glasner & J. W. Truran (2009) have reported breakout from the hot CNO cycle for very low accretion rates of $M_{\text{acc}} = 10^{-11} M_{\odot} \text{ yr}^{-1}$, which, however, are not supported by observations. The ability of low-metallicity nova models to develop a weak rp -process depends on two key factors: the high peak temperature ($T_{\text{peak}} > 3 \times 10^8 \text{ K}$) and, more importantly, the mixing between the low-metallicity envelope and the outer layers of the white dwarf. The low metallicity of the accreted material results in reduced nuclear activity during the accretion phase, prolonging its duration and allowing more mass to accumulate. This leads to higher pressures at the base of the envelope. A key factor in this context is the time required for the envelope to become fully convective, as this marks the onset of dredge up. Once convection sets in, fresh ^{12}C is mixed into the envelope, creating thermodynamic conditions favorable for a powerful explosion and enabling the envelope to reach the high peak temperatures required for ignition. The explosion is then triggered by the $^{12}\text{C}(p, \gamma)^{13}\text{N}$ reaction, initiating the thermonuclear runaway.

For model Z1e-7, the reaction flow cannot proceed beyond $A = 67$ and ^{67}Ge β^+ decays back to ^{67}Zn , while for models Z2e-6 and Z2e-5, the endpoint is slightly lower in mass number. The lowest-metallicity nova (model Z2e-9) exhibits a weak rp -process with the shortest nucleosynthesis endpoint around cobalt, the maximum element where $\log_{10}(X_i/X_{\odot}) > 0$. This is due to its helium-rich composition (initially $X(\text{H}) = 0.314$ and $X(\text{He}) = 0.371$; see Table 4 in the Appendix for the full initial mass fractions; these should not be confused with the composition of the outermost layers of the ONe white dwarf, which are provided in Table 2), and the temperature is not high enough for α -capture reactions to move the reaction flow to heavier masses. This behavior is likely a numerical artifact of the one-zone approach, which lacks the convective mixing present in hydrodynamic models, leading to an insufficient amount of hydrogen fuel. In realistic conditions, convection replenishes hydrogen in the envelope by mixing material from cooler regions. Hydrodynamic simulations of low-metallicity novae consistently show that protons are not consumed entirely, enabling continued nucleosynthesis.

4. The Impact of Thermonuclear Reaction Rate Uncertainties

Monte Carlo sensitivity studies are widely used in the literature for a variety of nucleosynthesis scenarios, e.g., Big Bang nucleosynthesis (C. Iliadis & A. Coc 2020), X-ray bursts (A. Parikh et al. 2008), νp -process (N. Nishimura et al. 2019), s -process (G. Cescutti et al. 2018), r -process (M. R. Mumpower et al. 2016), weak r -process (A. Psaltis et al. 2022), i -process (P. A. Denissenkov et al. 2021), and the γ -process (T. Rauscher et al. 2016). Monte Carlo studies offer several advantages over traditional methods for assessing the impact of nuclear physics uncertainties in astrophysical environments, such as individually varying reaction rates (e.g., C. Iliadis et al. 2002). They allow a full propagation of nuclear physics uncertainties to final abundances, which can be summarized with statistically meaningful metrics. They also naturally include the possible impact of multiple reactions impacting the nucleosynthesis of an isotope: while one rate might significantly alter an abundance, a second rate could either compensate for or amplify this change.

We evolve our reaction network, detailed in Section 3, using the thermodynamic conditions outlined in Section 2, initiating our calculations at the peak temperature (T_{max} , Table 1) to preserve hydrogen fuel until the onset of the thermonuclear runaway. This approach serves as a tool for performing one-zone postprocessing calculations while ensuring consistency with the results obtained using the hydrodynamic code SHIVA.

Each model underwent 10,000 postprocessing nucleosynthesis calculations, varying reaction rates based on the uncertainties listed in the STARLIB rate library (A. L. Sallaska et al. 2013). The reaction rates in STARLIB have lognormal probability densities at each temperature T and can be described by

$$f(r) = \frac{1}{\sigma\sqrt{2\pi}} \frac{1}{r} e^{-(\ln r - \mu)^2 / (2\sigma^2)}, \quad \text{for } 0 < r < \infty, \quad (2)$$

where r is the reaction rate. The recommended (median), low, and high rates are given by $r_{\text{median}} = e^{\mu}$, $r_{\text{low}} = e^{\mu - \sigma}$, and $r_{\text{high}} = e^{\mu + \sigma}$, respectively (R. Longland et al. 2010). The factor uncertainty ($f.u.$), which determines the 68% coverage probability, is given by $f.u. = e^{\sigma}$ (C. Iliadis et al. 2015).

In each Monte Carlo calculation i , we assign a random variation factor p_{ij} to each nuclear interaction. This factor is drawn from a normal (Gaussian) distribution with a mean of $\mu = 0$ and a variance $\sigma^2 = 1$, i.e., $p_{ij} \sim N(0, 1)$, where $N(0, 1)$ denotes the standard normal distribution. This factor is then used to calculate the sampled rate of reaction j using the following:

$$r_{ij} = r_{\text{median},j} [f.u.]_j^{p_{ij}}. \quad (3)$$

For forward and reverse reactions, we apply the same variation exponent p . Each sampled reaction rate is multiplied by a factor $[f.u.]_j^{p_{ij}}$ at each temperature ($T = 0.01$ – 10 GK), maintaining the temperature dependence of the rate uncertainty. For a more detailed discussion regarding the sampling procedure in a Monte Carlo nucleosynthesis study, we refer the interested reader to R. Longland (2012).

To visually represent the above procedure, we show an example for the $^{39}\text{K}(p, \gamma)^{40}\text{Ca}$ reaction rate in Figure 3. In the top panel, four draws of the rate variation factor p , which is normally distributed, are illustrated. In the bottom panel, these points are translated into reaction rates that are compared with the median using Equation (3). For example, the blue point in

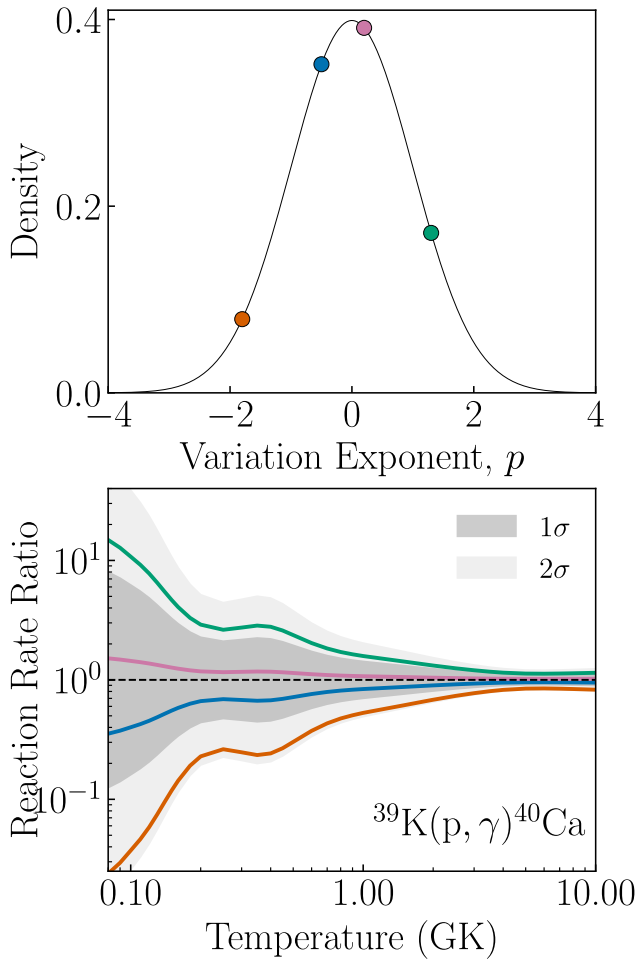


Figure 3. Top: four draws from the normal distribution for the variation factor p . Bottom: the resulting reaction rates compared to the median for the $^{39}\text{K}(p, \gamma)^{40}\text{Ca}$ reaction rate. See the main text for details.

the top panel of Figure 3 represents a sample with $p = -0.5$. Next, the sampled reaction rate is calculated using Equation (3), which yields the blue line in the bottom panel of Figure 3. The difference between the sampled and the median rate is not constant; it varies with the temperature-dependent uncertainty. Similar to the blue point, the orange, violet, and green points correspond to draws with $p = -1.8$, 0.2, and 1.3, respectively.

In the Monte Carlo nucleosynthesis framework, each reaction network calculation results in an abundance pattern, and their aggregate can help construct a probability density for each element or isotope. Figure 4 shows the final overproduction factors, $\log_{10}(X/X_{\odot})$, for the stable isotopes for all models with their 1σ uncertainty (68% coverage probability) from the variation of the thermonuclear reaction rates.

The impact of the thermonuclear reaction rate uncertainty is found by determining the correlation between the variation exponent p and the final mass fraction of an element X_k . In the present work, we use the mutual information (MI) metric, as it was first introduced for Monte Carlo nucleosynthesis in C. Iliadis & A. Coc (2020). It has the advantage, compared to commonly used metrics in Monte Carlo studies, such as the Pearson (linear; N. Nishimura et al. 2019) and Spearman (monotonic; A. Psaltis et al. 2022) correlation coefficients, to capture correlations that are neither linear nor monotonic.

For two random variables, in our analysis the simulated Monte Carlo mass fractions $\{X_{1k}, X_{2k}, X_{3k}, \dots\}$ and the sampled rates of the j th reaction, which are drawn based on its uncertainty, $\{r_{1j}, r_{2j}, r_{3j}, \dots\}$ the MI can be written as¹¹

$$\text{MI} = \sum_X \sum_r P(X, r) \log \left[\frac{P(X, r)}{P(X)P(r)} \right], \quad (4)$$

where $P(X)$ and $P(r)$ are, respectively, the marginal distributions of the mass fraction and the reaction rate, and $P(X, r)$ is the joint probability density.

For the results in Section 5, we use a critical limit of $\text{MI} = 0.09$ to define an “important” reaction, i.e., one whose uncertainty needs to be reduced. Since MI has no upper bound, we visually inspected the plots to identify meaningful changes in correlation. Figure 5 shows four example cases from model Z1e-7 (see Table 3 for a complete list), arranged according to the magnitude of the MI metric. The leftmost panel shows the variation of the $^{12}\text{C}(\alpha, \gamma)^{16}\text{O}$ reaction, which shows no visible correlation with the mass fraction of Ti. The second panel displays a small correlation with MI of less than 0.09. The last two examples correspond to reactions identified as “important” for the model, where a correlation can be clearly seen. It can be observed that below $\text{MI} = 0.09$, no correlation is discernible visually. Therefore, in this work, we use this cutoff to define an important reaction, and only these reactions are presented in the tables.

5. Results

This section highlights the key findings from our Monte Carlo sensitivity analysis.

5.1. Reactions That Affect Elemental Abundances

We present in Table 3 the reactions whose MI metric is above 0.09 for elements with a mean mass fraction $X_i > 10^{-10}$ and with abundance uncertainties of more than a factor of 3.

As expected, most identified reactions are proton captures, (p, γ) . The $^{15}\text{O}(\alpha, \gamma)^{19}\text{Ne}$ reaction, which is a breakout from the hot CNO cycles, affects the production of Co and Ni in multiple models because it controls how fast the material flows from the CNO region to heavier mass isotopes. The $^{18}\text{F}(p, \alpha)^{15}\text{O}$ closes the hot CNO cycle and affects the production of fluorine in models Z2e-6 and Z2e-5. The (p, γ) reactions on the following target nuclei affect multiple elements in many models: ^{30}P , $^{33,34}\text{S}$, ^{43}Sc , $^{44,46}\text{Ti}$, ^{50}Cr , ^{53}Mn , ^{54}Fe , ^{63}Cu , and $^{64,65}\text{Zn}$. For most of the aforementioned isotopes, the (p, γ) reaction rates are based on theoretical estimates using the statistical Hauser–Feshbach model, and no experimental data are available. In the STARLIB library, such reactions have an $f. u.$ of 10 for the whole temperature grid.

5.2. Signatures of Low-metallicity Nova Explosions

The imprint of low-metallicity nova explosions is an exciting yet underexplored topic in observational astrophysics. In this context, we will briefly discuss three potential ways to detect signatures of such explosions: through the study of GCs, extragalactic and galactic halo nova explosions, and presolar stardust grains.

High-resolution spectroscopy offers a powerful tool for investigating novae in low-metallicity environments. UV

¹¹ We use the `mutual_info_regression` module from the `scikit-learn` (F. Pedregosa et al. 2011) package to calculate the MI values.

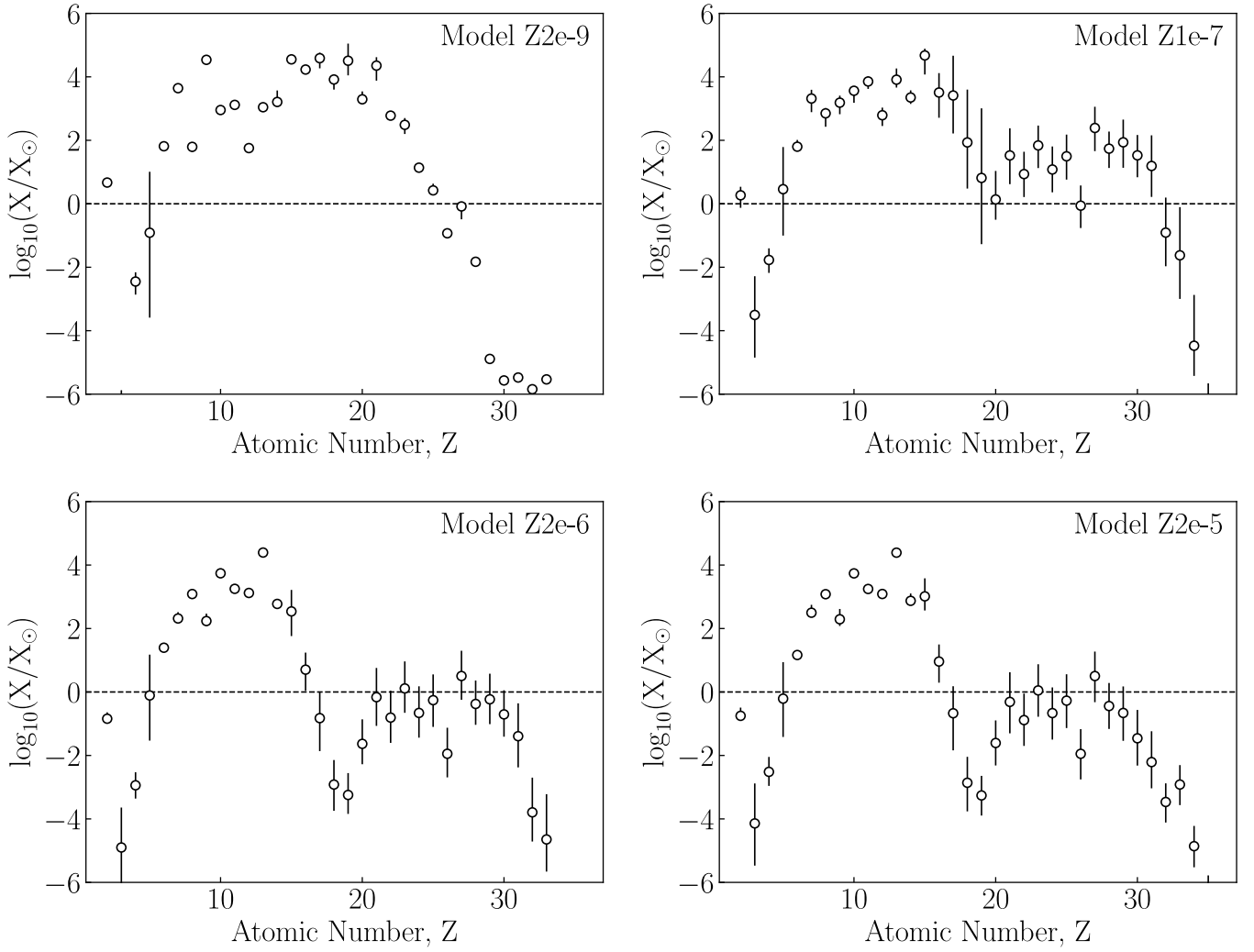


Figure 4. Overproduction plots for each model as a ratio of the logarithm of the abundance of each element to its solar value (K. Lodders 2020)— $\log_{10}(X/X_{\odot})$. The 1σ uncertainties (68% coverage probability) are due to the variation of thermonuclear reaction rates using a Monte Carlo sampling. See Section 4 for a detailed discussion.

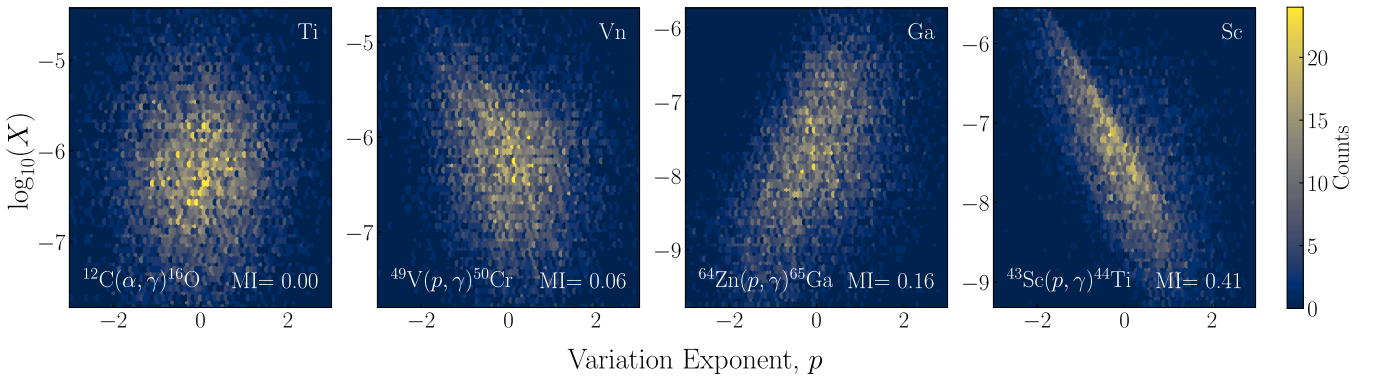


Figure 5. Correlations between elemental mass fractions and reaction rates for four representative cases in model Z1e-7. Each panel highlights a specific element (indicated in the top right corner: titanium, vanadium, gallium, and scandium) and the corresponding reaction with its MI value (displayed at the bottom). The panels are arranged in order of increasing MI value from left to right, illustrating the strength of the correlation. A reaction is considered “important” if its MI exceeds the threshold of 0.10, as no significant correlations are visually discernible for reactions with MI below this value.

observations can provide elemental yields, while near-IR spectroscopy offers limited isotopic information. Recently, A. Evans et al. (2024) reported the first IR observation of a recurrent nova in the LMC, identifying silicon emission lines.

GCs are ideal environments to study stellar populations and their nucleosynthesis (K. M. Ashman & S. E. Zepf 2008;

C. Iliadis et al. 2016), and they can provide a viable environment to detect low-metallicity novae, given that they host an older population of stars. Unfortunately, there have been only two confirmed nova detections in Galactic GCs: in M80 (T Sco 1660; H. B. Sawyer 1938) and in NGC 6402 (M14; H. Sawyer Hogg & A. Wehlauf 1964). Given the small

Table 3
Reactions with $MI \geq 0.09$ That Affect Isotopic Mass Fractions by More Than a Factor of 3 in Any Model

Reaction	Affected Element	Model Z2e-9 MI	Model Z1e-7 MI	Model Z2e-6 MI	Model Z2e-5 MI
$^{11}\text{B}(\alpha, n)^{14}\text{N}$	B	...	0.09	0.10	...
$^{11}\text{C}(\alpha, p)^{14}\text{N}\diamond$	B	0.20
$^{11}\text{C}(\alpha, n)^{14}\text{O}\diamond$	B	0.11	0.34	0.40	0.57
$^{15}\text{O}(\alpha, \gamma)^{19}\text{Ne}\diamond$	Fe	...	0.09	...	0.10
	Ni	...	0.19	0.11	0.11
	Co	...	0.11	...	0.09
	Ca	0.10
$^{17}\text{F}(p, \gamma)^{18}\text{Ne}\diamond$	N	...	0.16
	O	...	0.13
$^{18}\text{F}(p, \alpha)^{15}\text{O}\diamond$	F	0.16
$^{30}\text{P}(p, \gamma)^{31}\text{S}\diamond$	Si	1.19
	Cl	0.20	...	0.19	0.17
	S	...	0.25	0.78	0.64
	P	...	0.54	0.76	0.23
	Ar	0.14	0.14
$^{33}\text{S}(p, \gamma)^{34}\text{Cl}$	Cl	0.14	...	0.14	0.11
	Ar	0.09	0.09
$^{34}\text{S}(p, \gamma)^{35}\text{Cl}$	Cl	0.12	...	0.18	0.15
	Ar	0.14	0.11
$^{37}\text{Ar}(p, \gamma)^{38}\text{K}\diamond$	K	0.15
$^{38}\text{K}(p, \gamma)^{39}\text{Ca}\diamond$	K	0.54	0.09
$^{39}\text{K}(p, \gamma)^{40}\text{Ca}$	K	0.13	...	0.16	0.13
$^{42}\text{Ca}(p, \gamma)^{43}\text{Sc}$	Sc	0.20
$^{43}\text{Ca}(p, n)^{43}\text{Sc}$	Sc	0.13
$^{43}\text{Sc}(p, \alpha)^{40}\text{Ca}\diamond$	Ca	0.08	0.09
$^{43}\text{Sc}(p, \gamma)^{44}\text{Ti}\diamond$	Sc	0.20	0.41	0.20	0.35
	Ca	0.09	...
$^{44}\text{Ti}(p, \gamma)^{45}\text{V}\diamond$	Ti	...	0.16	0.11	0.11
$^{45}\text{Ti}(p, \gamma)^{46}\text{V}\diamond$	Sc	...	0.13
$^{46}\text{Ti}(p, \gamma)^{47}\text{V}$	V	0.31
	Ti	...	0.12	0.09	0.09
$^{47}\text{Ti}(p, n)^{47}\text{V}$	V	0.28
$^{47}\text{V}(p, \gamma)^{48}\text{Cr}\diamond$	V	0.09
$^{48}\text{V}(p, n)^{48}\text{Cr}\diamond$	V	0.09
$^{49}\text{V}(p, \gamma)^{50}\text{Cr}\diamond$	V	0.10
$^{48}\text{Cr}(p, \gamma)^{49}\text{Mn}\diamond$	Cr	...	0.11
$^{50}\text{Cr}(p, \gamma)^{51}\text{Mn}$	Cr	...	0.15	0.12	0.12
$^{52}\text{Mn}(p, \gamma)^{53}\text{Fe}$	Mn	...	0.11	...	0.09
$^{53}\text{Mn}(p, \gamma)^{54}\text{Fe}\diamond$	Mn	...	0.16	0.13	0.14
$^{54}\text{Fe}(p, \gamma)^{55}\text{Co}$	Fe	...	0.18	0.12	0.12
$^{55}\text{Co}(p, \gamma)^{56}\text{Ni}\diamond$	Co	...	0.18
$^{63}\text{Cu}(p, \gamma)^{64}\text{Zn}$	Cu	...	0.09	0.13	...
	Zn	...	0.11	0.16	0.13
$^{64}\text{Zn}(p, \gamma)^{65}\text{Ga}$	Ga	...	0.16	0.12	...
$^{65}\text{Zn}(p, \gamma)^{66}\text{Ga}\diamond$	Ga	...	0.16	0.15	...
$^{70}\text{Ge}(p, \gamma)^{71}\text{As}$	As	...	0.09

Note. The reactions indicated with a \diamond include a radioactive target nucleus.

statistics, the inferred frequencies for novae in GCs vary widely from $5 \times 10^{-4} \text{ yr}^{-1} \text{ GC}^{-1}$ (T. F. Doyle et al. 2019) to $0.05 \text{ yr}^{-1} \text{ GC}^{-1}$ (M. Henze et al. 2013).

In addition to the Magellanic Clouds, the Milky Way halo and its surrounding dwarf galaxies are also expected to host low-metallicity binaries. Our results, particularly those in Figure 4, suggest that low-metallicity nova explosions can overproduce a wide range of elements. However, significant nuclear physics uncertainties (Section 4) currently limit the precision with which we can constrain their contributions. High-resolution spectroscopic observations hold promise for identifying the chemical imprints of these explosions. In cases where isotopic abundances can be extracted through high-

resolution IR spectroscopy, even tighter constraints on this nucleosynthesis scenario could be achieved.

Regarding presolar stardust grains (S. Amari et al. 2001; E. Zinner 2014), J. José et al. (2007) proposed that models Z1e-7 (A) and Z2e-6 (B) could explain some unusual isotopic ratios found in Type-X grains. The models we computed in this work yield very low $^{14}\text{N}/^{15}\text{N}$ ratios, even smaller than those observed in SiC-X grains, while reproducing the $^{26}\text{Al}/^{27}\text{Al}$ and $^{30}\text{Si}/^{28}\text{Si}$ ratios within the uncertainties, based on the variation of reaction rates. For titanium isotopes, all models predict substantial production of ^{44}Ti and ^{46}Ti relative to stable ^{49}Ti . Our results agree with J. José et al. (2007); however, we cannot draw any definite conclusion due to the significant nuclear physics

uncertainties. Presolar grains are expected to survive in the interstellar medium for roughly 1 Gy before being incorporated into the presolar cloud about 4.8 Gy ago. This implies that any grain originating from a low-metallicity nova would have had to condense no more than 5.8 Gy ago. While the Milky Way has likely experienced at least two infall events (E. Spitoni et al. 2021), the likelihood of a nova explosion in a low-metallicity binary significantly contributing to the pollution of the protosolar nebula remains low. Nonetheless, given these uncertainties, such an event is not entirely out of the question.

6. Conclusions and Discussion

Low-metallicity novae are intriguing astrophysical environments that can produce elements up to Cu–Zn in metal-poor environments (Galactic halo, LMC, SMC, dwarf galaxies, and GCs), including the early history of the Milky Way.

In the framework of the present work, we explored the nucleosynthesis that occurs in that scenario, using four models based on 1D hydrodynamic models calculated with the code SHIVA. Their nucleosynthesis flow surpasses that of standard, classical novae and resembles a weak *rp*-process, which has only been reported in accreting neutron stars. We also studied the impact of thermonuclear reaction rate uncertainties using a Monte Carlo approach, identifying several reactions that need to be further investigated experimentally. While more advanced multidimensional methods are now feasible (J. Casanova et al. 2016; J. José et al. 2020), they fall outside the scope of this study. We show that, by adding a simple mixing scheme, 1D models can be used to capture the impact of nuclear physics uncertainties on this nucleosynthesis scenario.

Although low-metallicity nova explosions have yet to be observed, we anticipate that, in light of the findings presented in this work, a more systematic effort to target novae in GCs, the Galactic halo, and dwarf galaxies—using current and future space-based telescopes—will provide valuable high-resolution spectroscopic data. These observations will offer a unique opportunity to compare and refine our nucleosynthesis models.

The goal of the nuclear physics community should be to reduce the uncertainties of the reactions highlighted in Table 3, with upcoming experiments at stable and radioactive ion beam facilities to illuminate the low-metallicity nova contribution to the Galactic matter inventory.

Acknowledgments

The TUNL authors acknowledge support from U.S. Department of Energy, Office of Science, Office of Nuclear Physics, under Award Number DE-SC0017799 and contract Nos. DE-FG02-97ER41033 (TUNL), DE-FG02-97ER41041 (UNC), and DE-FG02-97ER41042 (NCSU). J.J. acknowledges support from the Spanish MINECO grant PID2023-148661NB-I00, the E.U. FEDER funds, and the AGAUR/Generalitat de Catalunya grant SGR-386/2021. The authors would like to thank S. Shore and N. Evans for fruitful discussions.

Software: IPython (F. Pérez & B. E. Granger 2007), Jupyter (T. Kluyver et al. 2023), matplotlib (J. D. Hunter 2007), numpy (C. R. Harris et al. 2020), scikit-learn (F. Pedregosa et al. 2011), scientific color maps (F. Crameri 2023).

Appendix

Here we present the initial mass fractions from the different low-metallicity nova models as extracted from the hydrodynamic code SHIVA (Table 4), and the factor uncertainties of the elemental mass fractions based on our Monte Carlo study (Table 5).

Table 4
Initial Elemental Mass Fractions for the Different Low-metallicity Nova Models Extracted from the Hydrodynamic Code SHIVA at $T = T_{\text{max}}$

Element	Model Z2e-9	Model Z1e-7	Model Z2e-6	Model Z2e-5
H	3.77e-01	6.06e-01	6.23e-01	6.65e-01
He	3.96e-01	3.93e-01	3.93e-01	3.34e-01
Li	2.93e-27	4.06e-27	4.06e-27	4.60e-27
Be	9.11e-14	3.83e-12	3.83e-12	3.31e-12
B	5.84e-19	3.25e-17	3.25e-17	6.97e-17
C	2.18e-07	5.39e-09	5.39e-09	8.58e-10
N	8.52e-07	3.59e-08	3.59e-08	5.68e-09
O	6.60e-02	4.21e-04	4.21e-04	2.28e-04
F	8.80e-03	9.71e-09	9.71e-09	3.95e-09
Ne	3.31e-02	3.20e-08	3.20e-08	4.85e-08
Mg	3.61e-02	2.59e-10	2.59e-10	1.01e-09
Al	1.82e-04	3.07e-11	3.07e-11	5.00e-11
Si	2.74e-03	3.90e-11	3.90e-11	9.81e-11
P	1.07e-02	1.29e-10	1.29e-10	3.30e-10
S	3.01e-02	6.58e-10	6.58e-10	1.84e-09
Cl	2.07e-02	2.41e-10	2.41e-10	9.73e-10
Ar	5.80e-03	2.11e-10	2.11e-10	6.62e-10
K	6.55e-03	1.11e-09	1.11e-09	1.96e-09
Ca	6.69e-03	5.38e-07	5.38e-07	4.52e-07
Sc	1.17e-04	3.51e-09	3.51e-09	4.02e-09
Ti	9.98e-05	1.61e-08	1.61e-08	1.58e-08
V	3.56e-05	1.61e-08	1.61e-08	1.01e-08
Cr	1.44e-05	5.88e-07	5.88e-07	2.90e-07
Mn	2.26e-06	9.64e-06	9.64e-06	5.63e-07
Fe	6.23e-06	1.25e-05	1.25e-05	5.44e-06
Co	1.55e-07	1.01e-05	1.01e-05	2.16e-06
Ni	4.24e-08	5.00e-05	5.00e-05	1.38e-05
Cu	2.90e-11	1.48e-06	1.48e-06	3.16e-07
Zn	2.25e-13	6.02e-07	6.02e-07	2.68e-08
Ga	8.99e-15	2.93e-09	2.93e-09	3.79e-10
Ge	1.02e-14	2.92e-11	2.92e-11	1.47e-10
As	1.05e-15	1.34e-13	1.34e-13	1.80e-11
Se	9.69e-17	8.57e-15	8.57e-15	1.28e-12
Br	1.78e-24	5.52e-21	5.52e-21	5.82e-19
Kr	1.13e-28	5.26e-26	5.26e-26	3.19e-23
Rb	2.19e-33	2.19e-33
Sr	7.40e-34	7.40e-34

Note. This is the starting point of the postprocessing nucleosynthesis. For the composition of the outer layers of the white dwarf, see Table 2.

Table 5

Factor Uncertainties (84th/50th Percentile Ratio) of the Elemental Mass Fractions for the Studied Models

	Model Z2e-9	Model Z1e-7	Model Z2e-6	Model Z2e-5
Li
Be
B	83.4	21.3	19.4	14.1
C	1.2	1.6	1.1	1.1
N	1.0	1.9	1.6	1.8
O	1.3	1.5	1.0	1.0
F	1.1	1.7	1.7	2.1
Ne	1.2	1.3	1.0	1.0
Na	1.2	1.4	1.2	1.3
Mg	1.2	1.7	1.1	1.1
Al	1.2	2.3	1.0	1.0
Si	2.3	1.7	1.4	1.7
P	1.3	1.6	4.8	3.7
S	1.1	4.1	3.4	3.5
Cl	1.5	17.9	6.6	7.1
Ar	1.4	46.3	5.9	6.6
K	3.5	156.1	4.9	4.1
Ca	1.8	7.9	5.9	5.1
Sc	1.8	7.2	8.3	8.6
Ti	1.4	5.0	7.0	6.8
V	1.6	4.2	7.1	6.7
Cr	1.1	5.3	6.9	6.4
Mn	1.6	4.8	6.5	6.8
Fe	1.0	4.3	6.6	6.0
Ni	1.0	3.5	5.5	5.3
Co	1.1	4.7	6.2	5.9
Cu	...	5.2	6.4	6.8
Zn	...	4.4	5.7	7.8
Ga	...	9.2	10.9	...
Ge	...	12.7
As	...	33.0

Note. We report factor uncertainties only for mean mass fractions $> 10^{-10}$.**ORCID iDs**Athanasios Psaltis  <https://orcid.org/0000-0003-2197-0797>Jordi José  <https://orcid.org/0000-0002-9937-2685>Richard Longland  <https://orcid.org/0000-0001-7731-580X>Christian Iliadis  <https://orcid.org/0000-0003-2381-0412>**References**

Amari, S., Gao, X., Nittler, L. R., et al. 2001, *ApJ*, **551**, 1065

Ashman, K. M., & Zepf, S. E. 2008, *Globular Cluster Systems* (Cambridge: Cambridge Univ. Press)

Bishop, S., Azuma, R. E., Buchmann, L., et al. 2003, *PhRvL*, **90**, 162501

Casanova, J., José, J., García-Berro, E., Calder, A., & Shore, S. N. 2010, *A&A*, **513**, L5

Casanova, J., José, J., García-Berro, E., Calder, A., & Shore, S. N. 2011a, *A&A*, **527**, A5

Casanova, J., José, J., García-Berro, E., & Shore, S. N. 2016, *A&A*, **595**, A28

Casanova, J., José, J., García-Berro, E., Shore, S. N., & Calder, A. C. 2011b, *Natur*, **478**, 490

Casanova, J., José, J., & Shore, S. N. 2018, *A&A*, **619**, A121

Cescutti, G., Hirschi, R., Nishimura, N., et al. 2018, *MNRAS*, **478**, 4101

Chen, H.-L., Woods, T. E., Yungelson, L. R., et al. 2019, *MNRAS*, **490**, 1678

Chomiuk, L., Metzger, B. D., & Shen, K. J. 2021, *ARA&A*, **59**, 391

Cramer, F. 2023, *Scientific Colour Maps v8.0.1*, Zenodo, doi:10.5281/zenodo.8409685

Denissenkov, P. A., Herwig, F., Perdikakis, G., & Schatz, H. 2021, *MNRAS*, **503**, 3913

Doyle, T. F., Shara, M. M., Lessing, A. M., & Zurek, D. 2019, *ApJ*, **874**, 65

Evans, A., Banerjee, D. P. K., Geballe, T. R., et al. 2024, *MNRAS*, **536**, 1710

Fisker, J. L., Schatz, H., & Thielemann, F.-K. 2008, *ApJS*, **174**, 261

Glasner, S. A., Livne, E., & Truran, J. W. 1997, *ApJ*, **475**, 754

Glasner, S. A., Livne, E., & Truran, J. W. 2007, *ApJ*, **665**, 1321

Glasner, S. A., Livne, E., & Truran, J. W. 2012, *MNRAS*, **427**, 2411

Glasner, S. A., & Truran, J. W. 2009, *ApJL*, **692**, L58

Goriely, S., Hilaire, S., & Koning, A. J. 2008, *A&A*, **487**, 767

Harris, C. R., Millman, K. J., van der Walt, S. J., et al. 2020, *Natur*, **585**, 357

Hartwig, T., Bromm, V., Klessen, R. S., & Glover, S. C. O. 2015, *MNRAS*, **447**, 3892

Henze, M., Pietsch, W., Haberl, F., et al. 2013, *A&A*, **549**, A120

Hocdé, V., Smolec, R., Moskalik, P., Ziolkowska, O., & Singh Rathour, R. 2023, *A&A*, **671**, A157

Hunter, J. D. 2007, *CSE*, **9**, 90

Iliadis, C. 2015, *Nuclear Physics of Stars* (New York: Wiley)

Iliadis, C., Champagne, A., José, J., Starrfield, S., & Tupper, P. 2002, *ApJS*, **142**, 105

Iliadis, C., & Coc, A. 2020, *ApJ*, **901**, 127

Iliadis, C., Karakas, A. I., Prantzos, N., Lattanzio, J. C., & Doherty, C. L. 2016, *ApJ*, **818**, 98

Iliadis, C., Longland, R., Coc, A., Timmes, F. X., & Champagne, A. E. 2015, *JPhG*, **42**, 034007

José, J. 2016, *Stellar Explosions: Hydrodynamics and Nucleosynthesis* (Boca Raton, FL: CRC Press)

José, J., García-Berro, E., Hernanz, M., & Gil-Pons, P. 2007, *ApJL*, **662**, L103

José, J., & Hernanz, M. 1998, *ApJ*, **494**, 680

José, J., & Shore, S. N. 2008, in *Classical Novae*, ed. M. F. Bode & A. Evans (Cambridge: Cambridge Univ. Press), 121

José, J., Shore, S. N., & Casanova, J. 2020, *A&A*, **634**, A5

Keller, S. C., Bessell, M. S., Frebel, A., et al. 2014, *Natur*, **506**, 463

Kemp, A. J., Karakas, A. I., Casey, A. R., et al. 2024, *A&A*, **689**, A222

Klessen, R. S., & Glover, S. C. O. 2023, *ARA&A*, **61**, 65

Kluuyver, T., Ragan-Kelley, B., Pérez, F., et al. 2023, in *Positioning and Power in Academic Publishing: Players, Agents and Agendas*, ed. F. Loizides & B. Schmidt (Amsterdam: IOS Press), 87

Lodders, K. 2020, *Solar Elemental Abundances*, Oxford Research Encyclopedia of Planetary Science (Oxford: Oxford Univ. Press)

Longland, R. 2012, *A&A*, **548**, A30

Longland, R., Iliadis, C., Champagne, A., et al. 2010, *NuPhA*, **841**, 1

Longland, R., Martin, D., & José, J. 2014, *A&A*, **563**, A67

Maiolino, R., Übler, H., Perna, M., et al. 2024, *A&A*, **687**, A67

Mumpower, M. R., Surman, R., McLaughlin, G. C., & Aprahamian, A. 2016, *PrPNP*, **86**, 86

Nakajima, K., & Maiolino, R. 2022, *MNRAS*, **513**, 5134

Nishimura, N., Rauscher, T., Hirschi, R., et al. 2019, *MNRAS*, **489**, 1379

Parikh, A., José, J., Moreno, F., & Iliadis, C. 2008, *ApJS*, **178**, 110

Pedregosa, F., Varoquaux, G., Gramfort, A., et al. 2011, *JMLR*, **12**, 2825

Pérez, F., & Granger, B. E. 2007, *CSE*, **9**, 21

Piersanti, L., Cassisi, S., Iben, I., Jr., & Tornambé, A. 2000, *ApJ*, **535**, 932

Psaltis, A., Arcones, A., Montes, F., et al. 2022, *ApJ*, **935**, 27

Rauscher, T., Nishimura, N., Hirschi, R., et al. 2016, *MNRAS*, **463**, 4153

Ritossa, C., García-Berro, E., & Iben, I. J. 1996, *ApJ*, **460**, 489

Sallaska, A. L., Iliadis, C., Champagne, A. E., et al. 2013, *ApJS*, **207**, 18

Sawyer, H. B. 1938, *JRASC*, **32**, 69

Sawyer Hogg, H., & Wehlau, A. 1964, *JRASC*, **58**, 163

Schatz, H., Aprahamian, A., Goerres, J., et al. 1998, *PhR*, **294**, 167

Shafter, A. W. 2017, *ApJ*, **834**, 196

Shen, K. J., & Bildsten, L. 2007, *ApJ*, **660**, 1444

Shen, K. J., & Bildsten, L. 2009, *ApJ*, **692**, 324

Spitoni, E., Verma, K., Silva Aguirre, V., et al. 2021, *A&A*, **647**, A73

Stacy, A., & Bromm, V. 2013, *MNRAS*, **433**, 1094

Stacy, A., Bromm, V., & Lee, A. T. 2016, *MNRAS*, **462**, 1307

Starrfield, S., Bose, M., Iliadis, C., et al. 2020, *ApJ*, **895**, 70

Starrfield, S., Iliadis, C., & Hix, W. R. 2008, in *Classical Novae*, ed. M. F. Bode & A. Evans (Cambridge: Cambridge Univ. Press), 77

Starrfield, S., Iliadis, C., & Hix, W. R. 2016, *PASP*, **128**, 051001

Starrfield, S., Schwarz, G., Truran, J. W., & Sparks, W. M. 2000, in *AIP Conf. Ser. 522, Cosmic Explosions: Tenth Astrophysics Conf.*, ed. S. S. Holt & W. W. Zhang (Melville, NY: AIP), 379

Starrfield, S., Timmes, F. X., Iliadis, C., et al. 2012, *BaltA*, **21**, 76

van Wormer, L., Görres, J., Iliadis, C., Wiescher, M., & Thielemann, F. K. 1994, *ApJ*, **432**, 326

Wagoner, R. V. 1969, *ApJS*, **18**, 247

Wallace, R. K., & Woosley, S. E. 1981, *ApJS*, **45**, 389

Wiescher, M., Görres, J., Uberseder, E., Imbriani, G., & Pignatari, M. 2010, *ARNPS*, **60**, 381

Zinner, E. 2014, *Treatise on Geochemistry* (Amsterdam: Elsevier), 181